Acta Crystallographica Section B
Structural Science
ISSN 0108-7681

Persistence of the stereochemical activity of the Bi^{3+} lone electron pair in $Bi_2Ga_4O_9$ up to 50 GPa and crystal structure of the high-pressure phase

Alexandra Friedrich,[a]* Erick A. Juarez-Arellano,[a]‡ Eiken Haussühl,[a] Reinhard Boehler,[b]§ Björn Winkler,[a] Leonore Wiehl,[a] Wolfgang Morgenroth,[a,c] Manfred Burianek[d] and Manfred Mühlberg[d]

[a]Institut für Geowissenschaften, Goethe Universität Frankfurt, Altenhöferallee 1, D-60438 Frankfurt am Main, Germany, [b]Max-Planck Institut für Chemie, D-55020 Mainz, Germany, [c]c/o DESY/HASYLAB, D-22603 Hamburg, Germany, and [d]Institut für Kristallographie, Universität zu Köln, D-50674 Cologne, Germany

‡ Present address: Universidad del Papaloapan, Circuito Central 200, Parque Industrial, Tuxtepec 68301, México.
§ Present address: Geophysical Laboratory, Carnegie Institution of Washington, Washington, DC 20015, USA.

Correspondence e-mail: friedrich@kristall.uni-frankfurt.de

Received 19 January 2010
Accepted 17 March 2010

The crystal structure of the high-pressure phase of bismuth gallium oxide, $Bi_2Ga_4O_9$, was determined up to 30.5 (5) GPa from *in situ* single-crystal in-house and synchrotron X-ray diffraction. Structures were refined at ambient conditions and at pressures of 3.3 (2), 6.2 (3), 8.9 (1) and 14.9 (3) GPa for the low-pressure phase, and at 21.4 (5) and 30.5 (5) GPa for the high-pressure phase. The mode-Grüneisen parameters for the Raman modes of the low-pressure structure and the changes of the modes induced by the phase transition were obtained from Raman spectroscopic measurements. Complementary quantum-mechanical calculations based on density-functional theory were performed between 0 and 50 GPa. The phase transition is driven by a large spontaneous displacement of one O atom from a fully constrained position. The density-functional theory (DFT) model confirmed the persistence of the stereochemical activity of the lone electron pair up to at least 50 GPa in accordance with the crystal structure of the high-pressure phase. While the stereochemcial activity of the lone electron pair of Bi^{3+} is reduced at increasing pressure, a symmetrization of the bismuth coordination was not observed in this pressure range. This shows an unexpected stability of the localization of the lone electron pair and of its stereochemical activity at high pressure.

1. Introduction

$Bi_2M_4O_9$ (M = Al^{3+}, Ga^{3+}, Fe^{3+}) compounds belong to the family of sillimanite- and mullite-type crystal structures (Fischer & Schneider, 2005; Schreuer *et al.*, 2006). These materials exhibit interesting properties, for instance photoluminescence (Blasse & Ho, 1980; Volkov *et al.*, 1996; Volkov & Egorysheva, 1996) and oxygen ionic conductivity (Bloom *et al.*, 1992), especially if part of the Bi^{3+} is replaced by divalent cations, such as Sr^{2+}, Ca^{2+} and Ba^{2+} (Zha *et al.*, 2003). Similar to bismuth oxide, they are potential candidates for applications such as electrolytes of solid oxide fuel cells, oxygen sensors, gas-separation membranes and scintillators (Volkov & Egorysheva, 1996; Abrahams *et al.*, 1999; Zha *et al.*, 2003). It is known that chemical substitution and variation of the temperature have large effects on the electronic properties of $Bi_2M_4O_9$ compounds (Zha *et al.*, 2003) and that these compounds are stable at high temperatures up to $\sim$1350 K (Safronov *et al.*, 1971; Schreuer *et al.*, 2006).

This structural family is characterized by chains of edge-sharing octahedra extending parallel to the *c* axis. Alternating along [110], half of the octahedral chains are rotated clockwise, the other half counterclockwise (Fig. 1). In sillimanite (Al_2SiO_5, space group *Pbnm*, Fig. 1) and mullites *sensu stricto* ($Al_{4+2x}Si_{2-2x}O_{10-x}$, nominally $0.2 \leq x \leq 0.5$, space group

Pbam), the octahedra are occupied by aluminium. In sillimanite the octahedral chains are cross-linked *via* double chains of corner-sharing tetrahedral groups extending parallel to the *c* axis (Fig. 1; Kerrick, 1990). The tetrahedral groups are alternately occupied by silicon and aluminium. The crystal structures of mullites can be derived from that of sillimanite by removing some of the O atoms, which bridge the tetrahedral double chains in sillimanite. The number of oxygen vacancies corresponds to x in the general formula $Al_{4+2x}Si_{2-2x}O_{10-x}$. x is correlated to the substitution of Al^{3+} for Si^{4+} and accompanied by the formation of tetrahedral triclusters (Fischer & Schneider, 2005).

The crystal structure of $Bi_2Ga_4O_9$ was first solved with a reliability index of $R_1 = 0.185$ by Tutov & Markin (1970), where $R_1 = \sum \|F_o| - |F_c\| / \sum |F_o|$ based on observed structure factors F with values larger than $4\sigma(F_o)$, and was later on improved by Mueller-Buschbaum & de Beaulieu (1978) (R_1 = 0.1) and Filatov *et al.* (2006) (R_1 = 0.052). The structure is orthorhombic with space group *Pbam* (a = 7.93, b = 8.31, c = 5.92 Å, Z = 2, Fig. 1; Tutov & Markin, 1970; Filatov *et al.*, 2006). Half of the Ga^{3+} ions are tetrahedrally coordinated, the other half are octahedrally coordinated. The Bi^{3+} ion has a stereochemically active localized $6s^2$ lone electron pair in the crystal structure. Hence, the environment of the Bi^{3+} ion is strongly anisotropic with three strong bonds and one weaker Bi—O bond on one side, and the lone electron pair and two long, very weak Bi—O bonds on the other side (Abrahams *et al.*, 1999; Fig. 1). Similar to the sillimanite structure, chains of edge-sharing GaO_6 octahedra run parallel to the *c* axis (Fig. 1). The octahedral chains are linked *via* the highly asymmetric BiO_6 groups and *via* Ga_2O_7 diortho groups formed by corner-sharing GaO_4 tetrahedra.

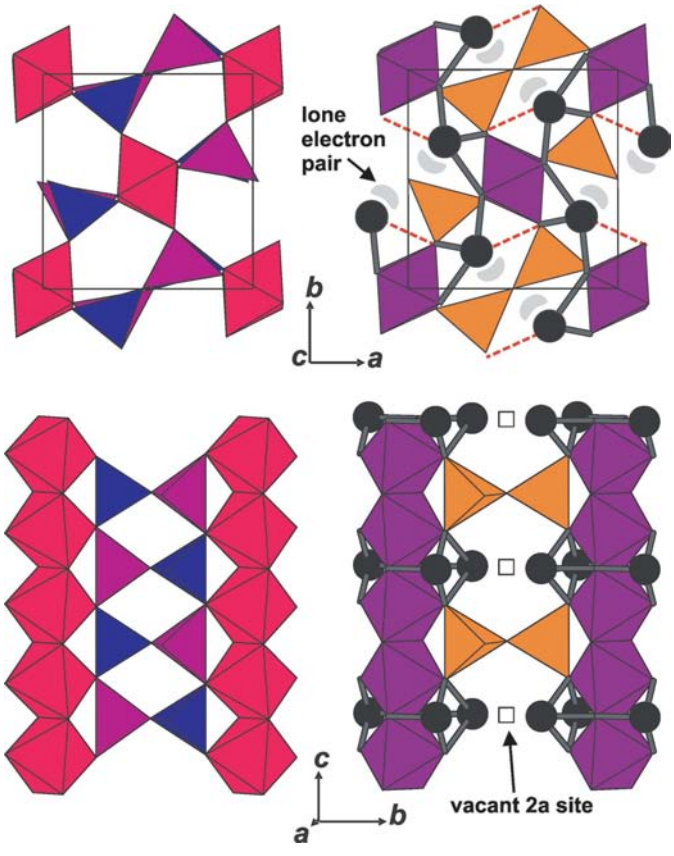

Figure 1
Crystal structures of sillimanite, Al_2SiO_5 (Burt *et al.*, 2006) (left) and $Bi_2Ga_4O_9$ (right) at ambient conditions. Dark grey (violet) octahedra represent GaO_6 groups (right) or AlO_6 groups (magenta, left). Light grey (orange) tetrahedra represent GaO_4 (right), dark (blue) and medium (violet) grey tetrahedra SiO_4 and AlO_4 groups (left), respectively. Bismuth atoms are drawn as black spheres. The two very weak Bi—O bonds are drawn by (red) dashed lines, while the approximate localization of the lone electron pairs of Bi^{3+} is drawn in light grey (top right). Vacant sites are created by the orientation of the lone electron pairs of two facing Bi^{3+} ions pointing towards these sites. The vacant sites (open squares) alternate with the central O atoms of the Ga_2O_7 dimers along the *c* axis (bottom right). This figure is in colour in the electronic version of this paper.

The Ga_2O_7 diortho groups are arranged in (001) planes, and alternate with planes of BiO_6 groups along the *c* axis. Hence, the central O atoms of the M_2O_7 dimers alternate along [001] with vacant sites. The lone electron pairs of two Bi^{3+} ions point towards these sites (Fig. 1; Abrahams *et al.*, 1999). The proposed mechanism of the oxygen-ion conductivity of isotypic $Bi_2Al_4O_9$ is based on this structural feature. The structural arrangement allows, in principle, the migration of those O atoms which connect the diortho groups. A relation of this mechanism to the large and extremely anisotropic atomic displacement ellipsoids of these O atoms was also proposed by Abrahams *et al.* (1999).

A detailed IR and Raman spectroscopic study on $Bi_2Ga_4O_9$ powder and oriented single crystals was recently published with the assignment of the vibrational modes (Beran *et al.*, 2008). Raman bands in the region below 300 cm^{-1} were mainly assigned to Bi—O stretching and bending modes, while Raman bands in the region between 300 and 800 cm^{-1} were assigned to Ga—O stretching and bending modes.

The strong anisotropy of the Bi^{3+} coordination often is the origin of interesting physical properties. For example, more than half of all noncentrosymmetric oxides contain lone electron pairs (Halasyamani & Poeppelmeier, 1998), and the noncentrosymmetry is a precondition for *e.g.* piezoelectricity, for optical activity and for optical second-harmonic generation. We are interested in the effect of pressure on the crystal structures of Bi^{3+} compounds like $Bi_2Ga_4O_9$, which contain lone electron pairs, as the lone electron pair is much more compressible and mobile with respect to space requirements of the bismuth coordination than the large anions surrounding the Bi^{3+} cation. Hence, it is generally assumed that the application of pressure will lead to an increase of the symmetry of the coordination sphere with a concomitant symmetrization of the electron distribution around the Bi^{3+} cation. This is accompanied by a decrease of the stereochemical activity of the lone electron pair such as has been reported earlier for the $4s^2$ electrons of Ge in $CsGeCl_3$ (Winkler *et al.*, 1998). If the pressure is high enough the lone electron pair will be forced into the *s* state, or a broadening or overlap of the valence and the conduction band will occur, which leads to semiconducting or metallic behaviour (Dinnebier *et al.*, 2003; Wang *et al.*, 2004).

An important measure for the stereochemical activity of the lone electron pair is the cation eccentricity (Balić Žunić & Makovicky, 1996). The eccentricity is defined by the deviation of the actual atom position from the center of the centroid of the surrounding ligands, divided by the average distance from the centroid to the ligands (Lundegaard *et al.*, 2003; Balić Žunić & Makovicky, 1996). A detailed experimental investigation of the effect of pressure on the stereochemical activity of the lone electron pairs of Bi^{3+} compounds has only been performed on a few Bi^{3+} sulfides up to now. *In situ* single-crystal structure analyses at pressures of up to 9 GPa have been reported for Bi_2S_3, bismuthinite (Lundegaard *et al.*, 2005), $PbBi_2S_4$, galenobismutite (Olsen *et al.*, 2007) and $Pb_3Bi_2S_6$, lillianite (Olsen *et al.*, 2008). The results on bismuthinite were complemented by semiquantitative calculations of the pressure dependence of the shape of the volume occupied by the lone electron pair (Lundegaard *et al.*, 2005). The eccentricities of the Bi^{3+} and Pb^{2+} ions are $e \simeq 0.15$ in bismuthinite (Lundegaard *et al.*, 2005), and $0.08 < e < 0.12$ and $0.04 < e < 0.10$ in galenobismutite (Olsen *et al.*, 2007) and lillianite (Olsen *et al.*, 2008). The Bi^{3+} cations are expected to show larger eccentricities and hence larger lone electron-pair activities than the Pb^{2+} cations, which is consistent with the assumed site occupancies at the Bi and Pb mixed sites of these sulfosalts. Another single-crystal structure analysis was reported for pressures up to 10 GPa for the lone-electron pair compound stibnite, Sb_2S_3, which is structurally related to bismuthinite (Lundegaard *et al.*, 2003). In stibnite the eccentricity of Sb^{3+} is $0.19 < e < 0.23$. A decrease of the eccentricity of Bi^{3+} and Sb^{3+} in their coordination polyhedra was observed with increasing pressure in these compounds, which is assumed to be correlated with the movement of the lone electron pair closer to the Bi^{3+} and Sb^{3+} ion. While in bismuthinite, galenobismutite and stibnite the pressure was not high enough to induce a phase transition, a reversible phase transition of first order was observed in lillianite between 3.7 and 4.9 GPa. The phase transition is accompanied by a rearrangement of some of the Pb^{2+} and Bi^{3+} lone electron pairs and an increase in their stereoactivity (Olsen *et al.*, 2008).

In a previous study we reported the bulk and linear compressibilities of $Bi_2Ga_4O_9$, isotypic $Bi_2Al_4O_9$ and structurally related $Bi_2Mn_4O_{10}$ up to pressures of 35 GPa by powder X-ray diffraction and up to 100 GPa by quantum-mechanical calculations using DFT (Lopéz-de-la Torre *et al.*, 2009). Apart from the fact that the compressibility is higher by $\sim 20\%$ in the DFT calcuations (Lopéz-de-la Torre *et al.*, 2009), which is explained by the underbinding due to the use of the generalized gradient approximation (GGA), the general trends agree reasonably well between experiment and theory. The results of the calculations indicated a change in the compression mechanism of $Bi_2Ga_4O_9$ in the pressure range between 15 and 25 GPa. This change was then confirmed experimentally for $Bi_2Ga_4O_9$, which undergoes a reversible phase transition at 16 GPa, by *in situ* powder synchrotron X-ray diffraction using the diamond–anvil cell technique. The phase transition is associated with a doubling of the *c* axis and hence of the unit-cell volume. This explains the failure of the DFT model to predict the correct high-pressure phase in the earlier study (Lopéz-de-la Torre *et al.*, 2009), as the imposition of periodic boundary conditions prevented the doubling of a cell parameter during the geometry optimization. The symmetry is reduced at the phase transition according to a group–subgroup relationship from the space group *Pbam* to the maximal non-isomorphic subgroup of type IIb *Pbnm* (with $c' = 2c$). $Bi_2Al_4O_9$ and $Bi_2Mn_4O_{10}$, however, do not show a phase transition up to the highest pressures studied. In this study we report the structural compression mechanism of $Bi_2Ga_4O_9$ up to the phase transition and the crystal structure of the high-pressure phase of $Bi_2Ga_4O_9$. The pressure evolution of the large eccentricity of the Bi^{3+} ion in this compound is discussed with respect to the phase transition and details of the electronic structure evolution with pressure are obtained from the evaluation of geometry relaxations using DFT. Vibrational properties of the low- and high-pressure phases are obtained from Raman spectroscopic measurements.

2. Experimental details

2.1. Sample preparation

The growth of $Bi_2Ga_4O_9$ single crystals is associated with steep liquidus curves in the growth range between 1200 and 1300 K. Due to incongruent melting the crystal growth had to be carried out from nonstoichiometric melts by the top-seeded solution growth (TSSG) method (Schreuer *et al.*, 2006; Burianek *et al.*, 2009). Resistance-heated three-zone Kanthal-A1 tube furnaces with crucible weighing devices were used for crystal growth. 4N (99.99%) Ga_2O_3 (ChemPur GmbH, Germany) and single-crystal grade Bi_2O_3 (Hek GmbH, Germany) in a ratio of 1:3 were inserted into Pt crucibles and thermally homogenized 20–50 K above the melting point for several days. Using a cooling rate of 3–10 K d^{-1} large, transparent, pale yellow single crystals with dimensions up to $\sim 20 \times 30 \times 10$ mm^3 were grown in 10–20 d. More details on the crystal growth are described in Burianek *et al.* (2009). Small single-crystal samples of $Bi_2Ga_4O_9$ have been obtained by cutting pieces from a large single crystal.

2.2. Single-crystal X-ray diffraction at ambient conditions

At ambient conditions intensity data were collected using an Xcalibur3 four-circle diffractometer from Oxford Diffraction equipped with a Sapphire3 CCD camera and a sealed tube with Mo $K\alpha$ radiation. A single crystal of $63 \times 54 \times 45$ μm^3 was used. The sample-to-detector distance was 42 mm and a total of 504 exposures (0.75° frame rotation, 120 s exposure time) were collected. Data reduction and absorption corrections were performed with the program *CrysAlis* (Oxford Diffraction, 2007). The starting atomic positions were obtained by direct methods using *SIR*2004 (Burla *et al.*, 2005) and the structure refinements were carried out with *SHELXL*97-2 (Sheldrick, 2008), both operated using the *WinGX* interface (Farrugia, 1999). The final refinement was carried out with anisotropic displacement parameters for all atoms. An extinction correction was applied. Experimental

Table 1
Experimental details.

For all structures: $Bi_2Ga_4O_9$, M_r = 840.84. Experiments were carried out at 293 K.

	Ambient	3.3 (2) GPa	6.2 (3) GPa	8.9 (1) GPa
Crystal data				
Crystal system, space group	Orthorhombic, *Pbam*	Orthorhombic, *Pbam*	Orthorhombic, *Pbam*	Orthorhombic, *Pbam*
a, *b*, *c* (Å)	7.9264 (4), 8.2922 (4), 5.8892 (3)	7.848 (6), 8.230 (5), 5.875 (3)	7.733 (2), 8.173 (10), 5.823 (1)	7.640 (2), 8.114 (9), 5.794 (1)
V (Å^3)	387.08 (3)	379.5 (4)	368.0 (5)	359.2 (4)
Z	2	2	2	2
Radiation type	Mo *Kα*	Mo *Kα*	Mo *Kα*	Mo *Kα*
μ (mm^{-1})	59.05	60.14	62.66	63.81
Crystal size (mm)	0.06 × 0.05 × 0.05	0.11 × 0.09 × 0.04	0.15 × 0.11 × 0.03	0.15 × 0.11 × 0.03
Data collection				
Diffractometer	Xcalibur3, Oxford Diffraction	Nonius CAD4	Nonius CAD4	Nonius CAD4
Absorption correction	–	Gaussian	Gaussian	Gaussian
T_{min}, T_{max}	–	0.277, 0.380	0.066, 0.113	0.062, 0.111
No. of measured, independent and observed [$I > 2\sigma(I)$] reflections	4550, 641, 609	1249, 413, 413	1467, 266, 266	1393, 263, 260
R_{int}	0.030	0.034	0.080	0.061
Refinement				
$R[F^2 > 2\sigma(F^2)]$, $wR(F^2)$, *S*	0.021, 0.051, 1.26	0.028, 0.077, 1.19	0.041, 0.106, 1.06	0.043, 0.117, 1.15
No. of reflections	641	413	266	263
No. of parameters	44	21	21	21
No. of restraints	6	0	0	0
$\Delta\rho_{max}$, $\Delta\rho_{min}$ (e Å^{-3})	2.57, −1.63	3.13, −3.05	4.39, −4.56	5.22, −5.80

	14.9 (3) GPa	21.4 (5) GPa	30.5 (5) GPa
Crystal data			
Crystal system, space group	Orthorhombic, *Pbam*	Orthorhombic, *Pbnm*	Orthorhombic, *Pbnm*
a, *b*, *c* (Å)	7.4596 (10), 8.058 (2), 5.747 (2)	6.966 (4), 8.155 (2), 11.49 (1)	6.705 (1), 8.107 (2), 11.393 (2)
V (Å^3)	345.4 (2)	652.7 (7)	619.3 (2)
Z	2	4	4
Radiation type	Synchrotron, λ = 0.45 Å	Synchrotron, λ = 0.45 Å	Synchrotron, λ = 0.45 Å
μ (mm^{-1})	20.15	21.32	22.48
Crystal size (mm)	0.04 × 0.03 × 0.01	0.05 × 0.04 × 0.02	0.05 × 0.04 × 0.02
Data collection			
Diffractometer	HUBER, D3, HASYLAB	HUBER, D3, HASYLAB	HUBER, D3, HASYLAB
Absorption correction	Gaussian	Gaussian	Gaussian
T_{min}, T_{max}	0.591, 0.521	0.554, 0.463	0.544, 0.448
No. of measured, independent and observed [$I > 2\sigma(I)$] reflections	769, 188, 145	1125, 348, 282	1396, 425, 340
R_{int}	0.077	0.060	0.070
Refinement			
$R[F^2 > 2\sigma(F^2)]$, $wR(F^2)$, *S*	0.048, 0.084, 1.11	0.051, 0.097, 1.15	0.036, 0.064, 1.15
No. of reflections	188	348	425
No. of parameters	20	31	36
No. of restraints	0	0	0
$\Delta\rho_{max}$, $\Delta\rho_{min}$ (e Å^{-3})	2.95, −3.28	3.32, −2.89	1.88, −2.74

Computer programs: *CrysAlis* (Oxford Diffraction, 2007), *CAD*4_0, *DIF*4 (Eichhorn, 1987), *Win-IntegrStp* (Angel, 2003), *ABSORB* (Angel, 2004), *AVSORT* (Eichhorn, 1978), *SIR*2004 (Burla *et al.*, 2005), *SHELXS*97, *SHELXL*97 (Sheldrick, 2008), *ATOMS* (Dowty, 1999).

details, crystal data and refinement results are summarized in Table 1 and unit-cell parameters from theory in Table 2.

2.3. Single-crystal X-ray diffraction at high pressure

Pressures up to 9 GPa were generated using two ETH-type diamond–anvil cells equipped with beryllium backing plates (Miletich *et al.*, 2000). The culet diameter was 600 µm. Single crystals (108 × 90× 40 µm^3 and 150 × 105 × 30 µm^3) were loaded together with ruby spheres, which were used for pressure determination by the laser-induced ruby-fluorescence technique, applying the pressure scale of Mao *et al.* (1986). A methanol–ethanol (4:1) mixture was used as a pressure-transmitting medium. Holes of ∼270 µm in

Table 2
Unit-cell parameters of $Bi_2Ga_4O_9$ at various pressures from theory.

p (GPa)	a (Å)	b (Å)	c (Å)	V (Å^3)
16	7.0955	8.3265	11.7016	691.34
18	7.0280	8.3070	11.6766	681.70
19	6.9995	8.2984	11.6624	677.41
20	6.9679	8.2896	11.6478	672.79
30	6.7430	8.2062	11.5105	636.93
35	6.6536	8.1657	11.4508	622.14
37	6.6223	8.1465	11.4281	616.53
40	6.5803	8.1151	11.3936	608.42
41	6.5656	8.1110	11.3822	606.14
44	6.5292	8.0827	11.3519	599.08
45	6.5171	8.0708	11.3429	596.62
50	6.4554	8.0286	11.2976	585.53

diameter, serving as pressure chambers, were drilled through steel (1.4310) gaskets (pre-indented to thicknesses of $\sim$ 86 µm) using a spark-eroding drilling machine.

For the generation of pressures between 15 and 30 GPa we used a Boehler–Almax diamond–anvil cell with an X-ray opening angle of 76° (Boehler, 2006). Small conical diamond anvils (Boehler & de Hantsetter, 2004) with beveled culets of $\sim$ 370 µm in diameter were glued to tungsten carbide seats. With this set-up the absorption of X-rays by the diamond–anvil cell components was minimized while maintaining maximal access to reciprocal space. The sample chambers were holes of 150 and 160 µm in diameter in tungsten gaskets of 136 µm initial thickness, which had been pre-indented to thicknesses of 43 and 36 µm. Single crystals of $Bi_2Ga_4O_9$ ($39 \times 26 \times 13$ µm^3 at 15 GPa and $40 \times 50 \times 20$ µm^3 at 21 and 31 GPa) were placed into the holes together with ruby chips for pressure determination. Compressed helium was used as pressure medium and was loaded into the pressure chamber at a pressure of 0.25 GPa within a pressure vessel.

The crystal quality had previously been checked at ambient conditions and was then checked at the loading pressure with the same in-house four-circle κ diffractometer as described above. While at pressures up to 15 GPa the peak hunting routine found enough reflections of $Bi_2Ga_4O_9$ for automatic indexing from the images (φ scan range of 40°), peaks had to be manually selected from the images at higher pressures (φ scan range of 80°), where the high-pressure phase is stable.

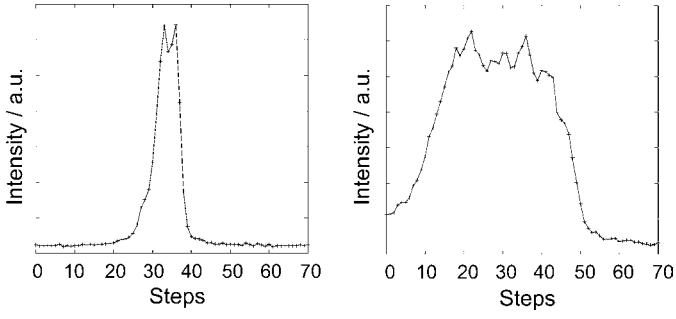

Figure 2
Reflection profile of the $(\bar{3}\bar{3}\bar{4})$ reflection at 30.5 (5) GPa (left) and after pressure release at 21.4 (5) GPa (right). The ω step width was 0.02° for both scans.

Table 3
Principal mean-square atomic displacements (Å^2).

Atom	L_1	L_2	L_3
Bi	0.0031	0.0053	0.0057
Ga1	0.0053	0.0025	0.0014
Ga2	0.0052	0.0026	0.0025
O1	0.0078	0.0038	0.0026
O2	0.0141	0.0024	0.0018
O3	0.0102	0.0034	0.0025
O4	0.0076	0.0338	0.0436

The unit cell of the high-pressure phase and the orientation matrix were determined from 224 reflections. The single crystal remained intact across the high-pressure phase transition.

Intensity data were collected in house at 3.3 (2), 6.2 (3) and 8.9 (1) GPa using a CAD4 kappa four-circle diffractometer from Enraf–Nonius equipped with a point detector and a sealed tube with Mo $K\alpha$ radiation. ω scans were measured applying the fixed-φ technique (Finger & King, 1978) in order to select the beam path of least attenuation through the pressure cell. The intensity data were examined and integrated using the program *Win-IntegrStp*, Version 3.5 (Angel, 2003).

At higher pressures [14.9 (3), 21.4 (5) and 30.5 (5) GPa] intensity data were collected at the bending-magnet beamline D3 at HASYLAB (Hamburg, Germany) using synchrotron X-ray radiation. Unit-cell parameters and intensity data were measured on a Huber four-circle diffractometer with an Euler geometry with an NaI point detector at a wavelength of 0.45 Å, provided by a Si(111) double-crystal monochromator. All accessible reflections within the Ewald sphere and at $\varphi = 0°$ were collected up to $2\theta = 15°$. From this measurement the reflection conditions could be derived and the most probable space group, *Pbnm*, could be determined. The list of accessible reflections with 2θ angles $> 15°$ and within an opening angle of 76° was manually shortened by removing the symmetry-forbidden reflections and reducing the maximum number of symmetry-equivalent reflections to four. Very weak reflections (*e.g.* due to high background intensity) were remeasured separately with scan times of up to 47 min. Intensity data were obtained from the scan data by the Lehmann–Larsen algorithm and corrected for Lorentz and polarization effects as well as intensity drifts of the primary beam using the beamline-adopted software *REDUCE* (Eichhorn, 1987) and *AVSORT* (Eichhorn, 1978).

The absorption of the X-ray beam by the sample and the diamond anvils was corrected with the program *ABSORB*, Version 6.0 (Angel, 2004). Structure determination of the high-pressure phase was carried out with *SHELXS*97-2 using the heavy-atom method, and structure refinements were performed with *SHELXL*97-2 (Sheldrick, 2008). The starting parameters for the refinements of the low-pressure phase were taken from structural data published by Mueller-Buschbaum & de Beaulieu (1978). The final refinements of the high-pressure data sets were carried out with isotropic displacement parameters for all atoms. Extinction corrections were applied at pressures below 10 GPa. The cation eccentricity was

calculated with the program *IVTON* (Balić Žunić & Vicković, 1996). Experimental details, crystal data and refinement results are summarized in Table 1.

About 2 months after the data collection at the highest pressure of 30.5 (5) GPa was performed one of the diamonds cracked, which caused a small pressure decrease down to 27.6 (1) GPa. However, the data quality after further pressure release to 21.4 (5) GPa diminished owing to peak broadening (Fig. 2), which might be due to the crystal bridging the diamonds. As a consequence, the structure was refined with the isotropic displacement parameters of all O atoms constrained to be equal at this pressure.

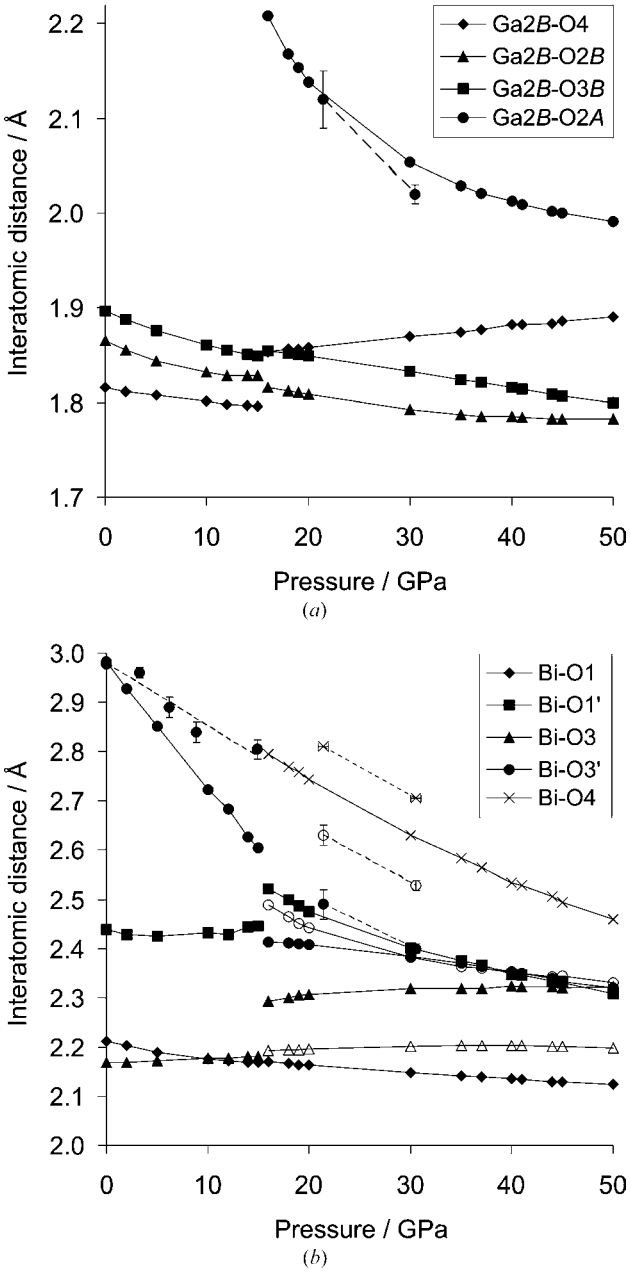

Figure 3
The pressure dependencies of the interatomic Ga2—O (*a*) and Bi—O (*b*) bond distances as obtained from theory show the increase of the polyhedra coordinations. For the sake of clarity, only the Ga2*B*—O bonds are drawn for the high-pressure phase, and only the experimentally derived Ga2*B*—O and Bi—O bond distances (symbols with error bars, dashed lines), which are responsible for the coordination increases. Bi—O bonds, which are non-symmetrically equivalent in the high-pressure phase, are distinguished by filled and open symbols.

2.4. Raman spectroscopy at high pressure

Micro-Raman measurements were performed with a Renishaw Raman spectrometer (RM-1000) equipped with a HeNe laser (633 nm, 50 mW). The system was calibrated using the band at 519 cm^{-1} of a silicon wafer (Temple & Hathaway, 1973). We employed a 20× objective lens with a long working distance. The sample was a single crystal, which was loaded in a Boehler–Almax diamond–anvil cell with helium as the pressure medium and also used for single-crystal X-ray diffraction. The pressure was decreased after X-ray intensity data collection from 27.6 (1) GPa (the highest pressure after one diamond broke) in steps of < 1 GPa to 21.8 (1) GPa and after a further X-ray measurement down to ambient pressure. The spectra were recorded in the range from 100 to 1000 cm^{-1} and with an exposure time of 100 s, except for the first measurement at 27.6 (1) GPa, which was exposed for 180 s. At most pressures spectra were recorded from the crystal in two mutually perpendicular orientations obtained after a rotation around the axis of the diamond–anvil cell. All spectra were corrected by subtracting a background and fitted to pseudo-Voigt functions using the program *DatLab* (Syassen, 2005).

3. Computational details

The quantum-mechanical calculations performed here were based on density-functional theory, DFT. While DFT itself is exact, practical calculations employing the Kohn Sham formalism require an approximation for the treatment of the exchange and correlation effects. Currently, the most widely used schemes are the generalized gradient approximation, GGA, or the local density approximation, LDA. All calculations reported here were performed with the GGA functional of Perdew, Becke and Ernzerhof (PBE; Perdew *et al.*, 1996), as implemented in the academic version of the *CASTEP* program (Clark *et al.*, 2005).

For the calculations ultrasoft pseudopotentials from the CASTEP database were employed. The cut-off for the kinetic energy was 380 eV. The spacing of the Monkhorst–Pack *k*-point grid was chosen to be smaller than 0.04 $Å^{-1}$, which had been shown to give converged results. We defined that self-consistency had been achieved when the residual stress was < 0.02 GPa, the maximal force < 0.01 eV $Å^{-1}$ and the energy change in the last self-consistent cycles was less than 5×10^{-6} eV per atom. All structural parameters not constrained by the space-group symmetry were relaxed simultaneously. Full geometry relaxations were performed for the $Bi_2Ga_4O_9$ crystal structure at seven pressures in the interval between 0 and 15 GPa. The compression mechanism and unit-cell parameters obtained from these calculations are reported in Lopéz-de-la Torre *et al.* (2009). Full geometry relaxations with

Table 4
Interatomic distances (Å) and polyhedral volumes (Å^3) from experimental data of $Bi_2Ga_4O_9$.

OQE and TQE are the octahedral and tetrahedral quadratic elongations, respectively.

p (GPa)	0.0001	3.3 (2)	6.2 (3)	8.9 (1)	14.9 (3)
Bi—O1	2.166 (4)	2.15 (1)	2.12 (6)	2.14 (7)	2.13 (2)
Bi—O1′	2.442 (5)	2.42 (2)	2.44 (5)	2.40 (6)	2.38 (2)
Bi—O3 2×	2.128 (4)	2.128 (4)	2.13 (1)	2.13 (1)	2.14 (3)
Bi—O3′ 2×	2.979 (4)	2.96 (1)	2.89 (2)	2.84 (2)	2.80 (3)
V	14.5 (1)	14.2 (1)	13.7 (4)	13.3 (4)	13.1 (3)
OQE	1.270 (5)	1.273 (5)	1.27 (1)	1.28 (1)	1.275 (8)
Eccentricity	0.281	0.278	0.265	0.246	0.235
⟨Bi—O⟩	2.469	2.455	2.433	2.414	2.400
Ga1—O2 2×	1.919 (4)	1.92 (1)	1.93 (3)	1.93 (3)	1.89 (2)
Ga1—O1 2×	2.000 (4)	2.02 (1)	2.00 (2)	1.97 (2)	1.98 (2)
Ga1—O3 2×	2.006 (4)	1.994 (9)	2.00 (4)	1.97 (4)	1.92 (1)
V	10.13 (7)	10.15 (7)	10.1 (2)	9.8 (2)	9.5 (1)
OQE	1.010 (2)	1.009 (5)	1.01 (2)	1.01 (2)	1.01 (1)
Eccentricity	0.028	0.034	0.021	0.014	0.031
⟨Ga1—O⟩	1.976	1.978	1.977	1.960	1.933
Ga2—O4	1.7917 (9)	1.783 (2)	1.766 (8)	1.762 (8)	1.751 (4)
Ga2—O2	1.847 (6)	1.85 (2)	1.81 (2)	1.80 (2)	1.79 (2)
Ga2—O3 2×	1.868 (4)	1.86 (1)	1.84 (2)	1.82 (2)	1.79 (4)
V	3.20 (3)	3.15 (3)	3.01 (6)	2.96 (5)	2.84 (7)
TQE	1.003 (6)	1.006 (7)	1.01 (2)	1.01 (2)	1.01 (2)
Eccentricity	0.029	0.029	0.027	0.024	0.015
⟨Ga2—O⟩	1.845	1.838	1.809	1.801	1.780

Table 5
Intrapolyhedral angles (°) and selected interpolyhedral angles (°) from experimental data of $Bi_2Ga_4O_9$.

p (GPa)	0.0001	3.3 (2)	6.2 (3)	8.9 (1)	14.9 (3)
O3—Bi—O3′	84.2 (2)	84.1 (6)	82.1 (8)	81.3 (7)	82 (2)
O3—Bi—O1 2×	86.1 (2)	84.1 (4)	82 (1)	81 (1)	80.4 (6)
O3′—Bi—O1 2×	72.1 (1)	72.2 (4)	73 (1)	72 (1)	70.6 (6)
O1—Bi—O1′	150.32 (9)	147.8 (4)	147 (1)	144 (1)	140.8 (4)
O4—Ga2—O2	112.9 (2)	112.5 (4)	115 (2)	114 (2)	111.3 (8)
O4—Ga2—O3 2×	112.5 (1)	113.8 (4)	113.3 (8)	113.7 (8)	116.5 (8)
O2—Ga2—O3 2×	104.8 (2)	103.3 (5)	101 (1)	101 (1)	100.3 (7)
O3—Ga2—O3′ 2×	108.8 (3)	109.2 (5)	111 (2)	112 (2)	110 (2)
O2—Ga1—O2′	84.3 (2)	83.7 (8)	86 (2)	86 (2)	86 (1)
O2—Ga1—O1 2×	97.8 (2)	97.2 (5)	96 (1)	97 (1)	96.6 (7)
O2′—Ga1—O1 2×	172.8 (2)	172.4 (6)	171 (2)	169 (2)	169 (1)
O1—Ga1—O1′	81.0 (2)	83.0 (8)	83 (2)	83 (2)	83 (1)
O2—Ga1—O3 2×	88.1 (2)	88.1 (5)	85 (2)	85 (1)	85 (1)
O2′—Ga1–O3′ 2×	95.9 (2)	95.7 (6)	99.4 (15)	99.5 (13)	99 (1)
O1—Ga1—O3 2×	91.1 (2)	91.9 (5)	89.9 (17)	91 (2)	93 (1)
O1′—Ga1—O3 2×	84.8 (2)	84.3 (5)	85.8 (18)	85 (2)	84 (1)
O3—Ga1—O3′	174.6 (2)	175.0 (6)	174.3 (7)	174.4 (7)	176 (3)
Bi—O1—Bi	138.9	141.3	141.2	141.5	144.6

the structural model of the high-pressure phase of $Bi_2Ga_4O_9$ were performed at 12 pressures between 16 and 50 GPa.

4. Results and discussion

Atomic coordinates and isotropic or equivalent displacement parameters of $Bi_2Ga_4O_9$ at ambient conditions and at pressures up to 30.5 GPa, ADPs at ambient conditions, the pressure dependence of the Raman band positions and the mode-Grüneisen parameters have been deposited.[1]

4.1. Crystal structure of $Bi_2Ga_4O_9$ at ambient conditions

The unit-cell parameters obtained from our single-crystal X-ray diffraction study at ambient conditions agree well with previously reported values (Tutov & Markin, 1970; Mueller-Buschbaum & de Beaulieu, 1978; Filatov *et al.*, 2006). Attempts to carry out numerical or semi-empirical absorption corrections did not improve the internal consistency of the data set. As the best refinements were obtained without applying an absorption correction, we conclude that although bismuth is a strong X-ray absorber, the small size of the single crystal and its quasi-isometric shape allow us to proceed without an absorption correction.

The refinement carried out with isotropic displacement parameters (IDPs) for all atoms results in IDP values close to the values reported by Filatov *et al.* (2006). The IDP value of the O4 atom, which is localized on a fully constrained position in the intersection of a twofold axis and a mirror plane (2/*m*), is around five times larger than the IDPs of the other O atoms. The same discrepancy of a factor of 5 was reported for the equivalent displacement factor of O4 in Filatov *et al.* (2006). When the refinement was carried out with anisotropic displacement parameters (ADPs), the mean-square displacement tensor of O4 became non-positive definite with one negative principal value (L_1) in the mirror plane, while the other two principal values were strongly extended. Hence, a weak restraint (ISOR) was applied on the O4 ADPs in order to prevent the generation of 'non-positive-definite' ADPs, which yielded principal mean-square atomic displacements (0.0076, 0.0338, 0.0436) with R_1 = 0.0212 (Table 3). A similar strongly anisotropic displacement ellipsoid of the O4 atom was also reported earlier (Filatov *et al.*, 2006). The R_1 value of our structure refinement is significantly lower than that of the earlier studies (Tutov & Markin, 1970; Mueller-Buschbaum & de Beaulieu, 1978; Filatov *et al.*, 2006).

The unusual behaviour of the O4 atom is not a result of the absence or wrong application of an absorption correction, which would affect all atoms, and most probably not due to the presence of a split position. The small principal mean-square atomic displacement value is oriented parallel to the straight Ga2—O4—Ga2 inter-tetrahedral angle, while the two elongated principal values are perpendicular to this direction. Hence, the strong anisotropy of the displacement ellipsoid seems to be due to static or dynamic disorder of the O4 atom, which connects the diortho group, from the fully constrained position, corresponding to a static or dynamic kink of the Ga2—O4—Ga2 angle. This hypothesis is in agreement with the fact that the Ga2—O4 bond is the shortest bond within the GaO_4 tetrahedron. To clarify this, temperature-dependent measurements are required and planned for the near future.

[1] Supplementary data for this paper are available from the IUCr electronic archives (Reference: SN5096). Services for accessing these data are described at the back of the journal.

4.2. Compression of the low-pressure structure up to 15 GPa

Bond distances and angles of $Bi_2Ga_4O_9$ between 0.0001 and 15 GPa are listed in Tables 4 and 5. A comparison of the compression mechanism of $Bi_2Ga_4O_9$ up to 15 GPa as obtained from experiment with that obtained from the DFT calculations shows good agreement. A key role in the compression mechanism are the changes in the environment of the stereochemically active Bi^{3+} ion. At ambient pressure the coordination of the Bi^{3+} ion is highly asymmetric due to the existence of the localized lone electron pair. With increasing pressure the distorted BiO_6 polyhedron does not become more symmetric with respect to an octahedral coordination as the octahedral quadratic elongation is independent of pressure (Table 4). Instead the lengths of the Bi—O bonds become more equal. While the three shortest Bi—O bonds ($\sim$ 2.15 Å at 1 bar) only change within 1.5 s.u.s up to 15 GPa and a fourth slightly longer bond [2.439 (7) Å] is shortened by $\sim$ 2.4%, the two significantly longer Bi—O3′ bonds [2.979 (7) Å] decrease by almost 6% (Table 4, Fig. 3). This behaviour is further reflected in the decreasing eccentricity of the Bi^{3+} ion (Fig. 4). The eccentricity, *e*, of the Bi^{3+} ion in $Bi_2Ga_4O_9$ (e = 0.281 at ambient conditions) is much larger than the eccentricity of Bi^{3+} and Pb^{2+} ions in the previously investigated bismuthinite ($e \simeq 0.15$; Lundegaard *et al.*, 2005), galenobismutite ($0.08 < e < 0.12$; Olsen *et al.*, 2007) and lillianite ($0.04 < e < 0.10$; Olsen *et al.*, 2008) or of the Sb^{3+} ions in stibnite ($0.19 < e < 0.23$; Lundegaard *et al.*, 2003). If one assumes that the position and extension of the lone electron pair will respond to pressure-induced space requirements of the crystal structure before the positions of the ligands change, a decrease of the eccentricity is expected for stereochemically active ions with increasing pressure accompanied by a decrease of the stereochemical activity of the ion. This is observed here (Fig. 4*a*). However, even after a pressure increase, the eccentricity of Bi^{3+} in $Bi_2Ga_4O_9$ is still larger (e = 0.235) than in the above-mentioned compounds at ambient conditions.

The two longest Bi—O bonds are oriented almost parallel to (010), inclined by $\sim$ 25° out of this plane. The strong compression of these bonds is the main reason for the high compressibility of the *a* axis, which is accompanied by a pressure-induced shift of the Bi^{3+} ions parallel to this axis, as indicated by the shift of the Bi *x* atomic coordinate. The Bi^{3+} ion, which is located on a mirror plane, cannot shift along the *c*

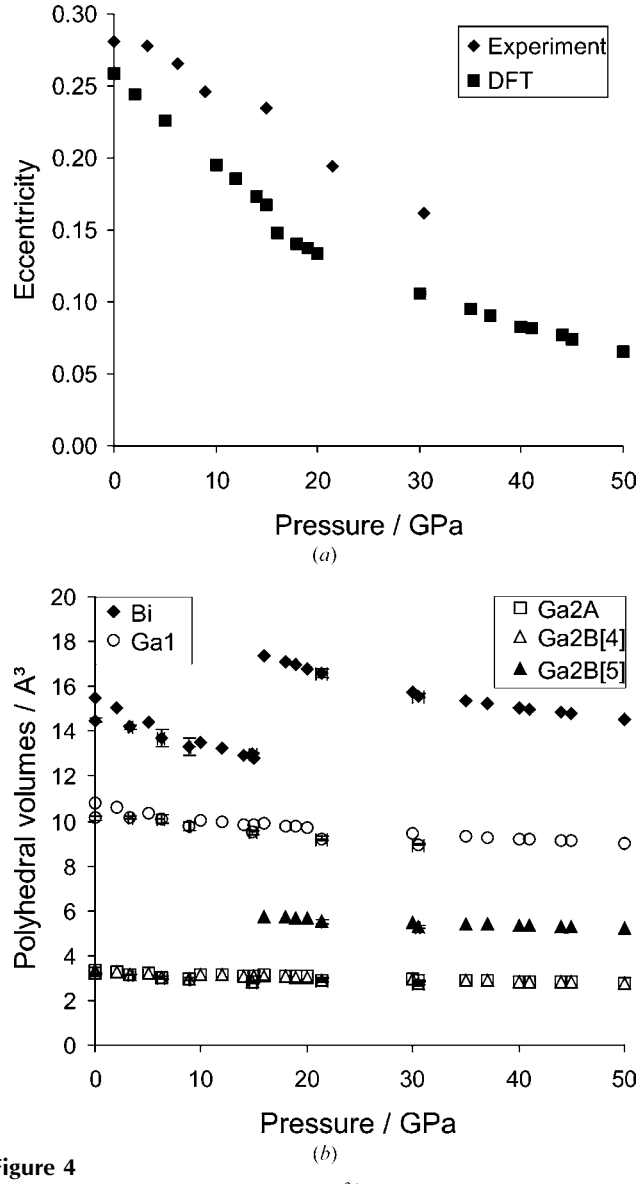

Figure 4
(*a*) Pressure dependence of the Bi^{3+} eccentricity from experiment (diamond) and theory (squares). (*b*) Pressure dependencies of the Bi and Ga polyhedral volumes from DFT and experiment (with error bars). The Ga2*A* and Ga2*B*[4] tetrahedral volumes coincide within the symbol size.

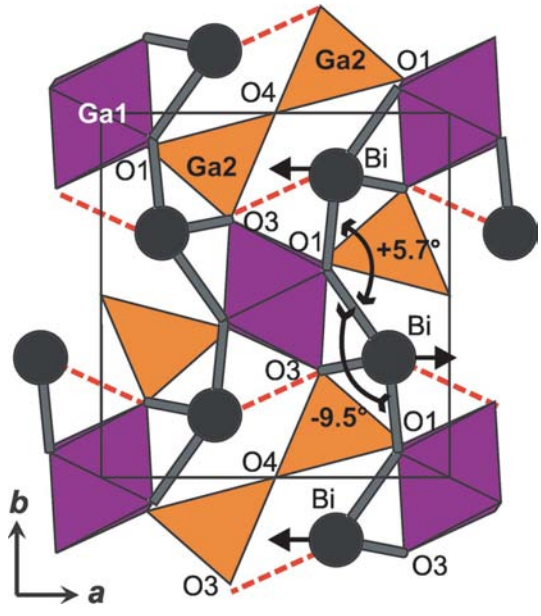

Figure 5
The structural compression of the low-pressure phase of $Bi_2Ga_4O_9$ is demonstrated with a projection of the crystal structure along the *c* axis. The longest Bi—O3′ bond indicated by red dashed lines is compressed by a movement of the Bi atom along the *a* axis. The changes in the Bi—O1—Bi and O1—Bi—O1′ angles are shown in the figure. This figure is in colour in the electronic version of this paper.

Table 6
Bulk moduli B (GPa) for the individual polyhedra of $Bi_2Ga_4O_9$ (DFT, this study) and the Al_2SiO_5 polymorphs (experiment).

Compound	X	Y	$B_{BiO_{6/7}}$	B_{XO_4}	B_{YO_6}	B_{YO_5}
$Bi_2Ga_4O_9$	Ga	Ga	61 (12)	153.3 (5)	131 (3)	–
$Bi_2Ga_4O_9$-HP	Ga	Ga	78 (4)	157 (1)	248 (4)	241 (2)
Sillimanite†	Al	Al	–	269 (33)	162 (8)	–
	Si	–	–	367 (89)	–	–
Andalusite‡	Si	Al	–	410 (150)	130 (20)	160 (50)
Kyanite§	Si	Al	–	322–400 (90)	207–281 (24)	–

† Yang *et al.* (1997*b*). ‡ Ralph *et al.* (1984). § Yang *et al.* (1997*a*).

axis without breaking the symmetry. The shift of the Bi^{3+} ions along the *a* axis also affects the changes of the intra- and interpolyhedral angles. Here again the largest changes are observed in the Bi environment. If we ignore the contribution of the two longer bonds (especially for low pressures), corrugated chains of the type·—Bi—O—Bi—O—· (Fig. 5) exist along the *b* axis. These chains show a strong bending of the O1—Bi—O1′ angle (150.3° at 0.0001 GPa, Table 5) by nearly 10° towards 140.8° at 15 GPa and a strong straightening of the Bi—O1—Bi angle by 5.7° with increasing pressure, associated with the movement of the Bi^{3+} ion along the *a* axis (Fig. 5). Owing to the opposed nature of the movements, the chains behave relatively stiffly upon compression.

The strong connectivity of the chains of GaO_6 octahedra running parallel to the *c* axis *via* shared edges is responsible for the low compressibility of this axis, which is reflected in the smaller compression of the bonds with edge-sharing O atoms (Ga1—O1 and Ga1—O2) if compared with those with non-edge-sharing atoms (Ga1—O3; Table 4). The compression of the GaO_4 tetrahedron is mainly achieved by bond compression, especially of the longest Ga2—O3 bonds, making the tetrahedron more regular with respect to the bond distances. This compression is associated with increasing deviations of the intra-tetrahedral O3—Ga2—O4 and O2—Ga2—O3 angles, which are increasing and decreasing, respectively, from the ideal tetrahedral angle of 109.5°.

Equation-of-state fits to the pressure dependencies of the polyhedral volumes obtained from experiment result in values with large uncertainties. As the experimental volumes are in good agreement with the polyhedral volumes obtained by theory (Fig. 4*b*), the discussion of the polyhedral compressibilities will be restricted to the theoretical results. Polyhedral volumes were fitted with Birch–Murnaghan equations-of-state of second order in the pressure range between 0 and 15 GPa, and bulk moduli are summarized in Table 6. The BiO_6 polyhedron is the most compressible, which is presumably related to the adaptabilty of the lone electron pair and the decrease of Bi^{3+} cation eccentricity at increasing pressure (Fig. 4). The GaO_6 octahedron is slightly more compressible than the GaO_4 tetrahedron, which is an expected result due to the higher coordination. In structurally related sillimanite a similar tendency is observed, *i.e.* the AlO_6 octahedron is more compressible than the AlO_4 and SiO_4 tetrahedra (Table 6; Yang *et al.*, 1997*b*). However, the GaO_4 and GaO_6 polyhedra in $Bi_2Ga_4O_9$ are more compressible than the corresponding AlO_6, AlO_4 and SiO_4 polyhedra (Table 6). A comparison of the Al_2SiO_5 polymorphs reveals a smaller compressibility of AlO_6 octahedra in the kyanite high-pressure structure (Table 6). The average bulk modulus reported for AlO_6 octahedra in oxides and silicates is $B_0(AlO_6)$ = 235 GPa ± 10% (Hazen *et al.*, 2000). In all the silicates the SiO_4 tetrahedra are very rigid with bulk moduli between 320 (Yang *et al.*, 1997*a*) and 580 GPa (*e.g.* for pyrope; Zhang *et al.*, 1998). The bulk moduli of the $M^{3+}O_6$ octahedra, M^{3+} = Al, Cr, Fe, V, Mn, of garnets are in the range between 167 and 213 GPa, as obtained from theoretical calculations (Milman *et al.*, 2001). Hence, the GaO_6 octahedron in $Bi_2Ga_4O_9$ is slightly more compressible than the MO_6 octahedra in the above-mentioned silicates, and the GaO_4 tetrahedron is much more compressible than AlO_4 and SiO_4 tetrahedra, which are rather incompressible.

Table 7
Interatomic distances (Å) and polyhedral volumes (Å^3) from experimental and DFT (*) data of the $Bi_2Ga_4O_9$ high-pressure phase.

OQE and TQE are the octahedral and tetrahedral quadratic elongations. For Ga2*B* both tetrahedral [4] and pyramidal [5] oxygen coordinations were considered.

p (GPa)	20*	21.4 (5)	30*	30.5 (5)	50*
Bi—O1	2.164	2.12 (2)	2.149	2.13 (1)	2.123
Bi—O1′	2.476	2.43 (2)	2.401	2.40 (1)	2.308
Bi—O3*A*	2.307	2.21 (3)	2.318	2.22 (1)	2.322
Bi—O3*A*′	2.408	2.49 (3)	2.384	2.40 (1)	2.321
Bi—O3*B*	2.196	2.09 (3)	2.201	2.09 (2)	2.108
Bi—O3*B*′	2.443	2.63 (2)	2.382	2.53 (1)	2.331
Bi—O4	2.743	2.813 (1)	2.631	2.705 (5)	2.460
V	16.812	16.6 (2)	15.731	15.58 (8)	14.534
Eccentricity	0.133	0.194	0.106	0.163	0.066
⟨Bi—O⟩	2.391	2.40	2.352	2.35	2.282
Ga1—O2*B*	1.875	1.81 (2)	1.866	1.81 (1)	1.876
Ga1—O1	1.967	1.92 (3)	1.954	1.94 (1)	1.933
Ga1—O1′	1.983	1.97 (3)	1.962	1.95 (1)	1.924
Ga1—O3*A*	1.963	1.91 (2)	1.927	1.897 (9)	1.877
Ga1—O3*B*	1.980	1.94 (2)	1.965	1.91 (1)	1.948
Ga1—O2*A*	2.011	2.00 (2)	1.998	1.963 (9)	1.956
V	9.73	9.2 (1)	9.44	8.97 (5)	9.01
OQE	1.025	1.02 (2)	1.027	1.03 (1)	1.031
Eccentricity	0.029	0.050	0.029	0.038	0.028
⟨Ga1—O⟩	1.963	1.93	1.945	1.91	1.919
Ga2*A*—O4	1.822	1.79 (3)	1.813	1.79 (1)	1.804
Ga2*A*—O2*A*	1.852	1.81 (3)	1.841	1.84 (1)	1.830
Ga2*A*—O3*A* 2×	1.852	1.82 (3)	1.835	1.80 (1)	1.810
V	3.07	2.92 (8)	2.95	2.87 (3)	2.76
TQE	1.032	1.02 (2)	1.045	1.04 (1)	1.070
Eccentricity	0.012	0.008	0.011	0.020	0.012
⟨Ga2*A*—O⟩	1.845	1.81	1.831	1.81	1.814
Ga2*B*—O4	1.859	1.81 (3)	1.870	1.80 (1)	1.890
Ga2*B*—O2*B*	1.809	1.82 (3)	1.793	1.77 (2)	1.783
Ga2*B*—O3*B* 2×	1.849	1.82 (3)	1.833	1.81 (2)	1.799
Ga2*B*—O2*A*	2.139	2.12 (3)	2.054	2.02 (1)	1.991
V [4]	3.04	2.91 (7)	2.94	2.77 (4)	2.79
V [5]	5.65	5.5 (1)	5.49	5.25 (6)	5.22
TQE	1.037	1.04 (2)	1.049	1.05 (1)	1.071
Eccentricity [4]	0.012	0.003	0.029	0.018	0.045
⟨Ga2*B*—O⟩ [4]	1.844	1.818	1.832	1.80	1.818
Eccentricity [5]	0.084	0.079	0.070	0.065	0.069
⟨Ga2*B*—O⟩ [5]	1.889	1.878	1.877	1.842	1.852

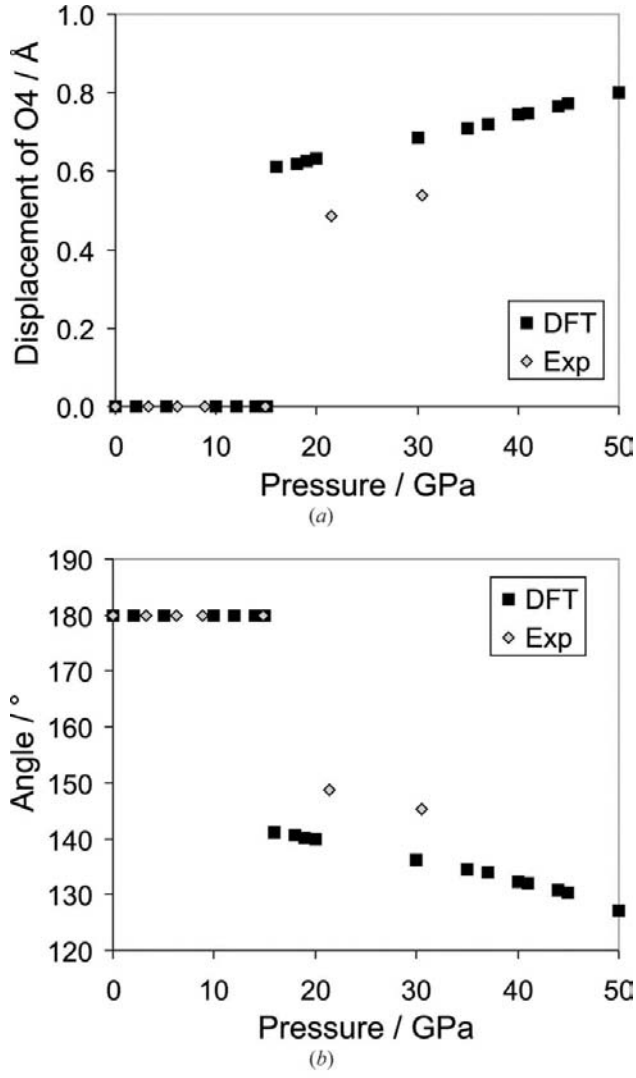

Figure 6
Pressure dependencies of the O4 displacement (*a*) and of the Ga2—O4—Ga2 interpolyhedral angle (*b*) from experiment (grey diamonds) and theory (solid squares). At the phase transition at 16 GPa a strong displacement and kinking are observed, which are enhanced with increasing pressure in the high-pressure phase.

4.3. Crystal structure of the high-pressure phase of $Bi_2Ga_4O_9$

The crystal structure of the high-pressure phase was solved using the 30.5 (5) GPa data and refined using the data collected at 21.4 (5) GPa. The doubled unit cell and space group *Pbnm* proposed for the high-pressure phase (Lopéz-de-la Torre *et al.*, 2009) were confirmed by the indexing of all reflections with the proposed unit cell and by checking the extinction rules (Table 1). No splitting of reflections arising from the phase transition was observed. Interatomic distances are listed in Table 7.

The most pronounced ion movement at the phase transition is observed for the O4 atom. Disorder at this atom position was already indicated by the strongly anisotropic displacement parameters at ambient conditions and the large isotropic displacement parameters at pressures below the phase transition. At pressures above the phase transition O4 was displaced from its fully constrained special position of Wyckoff notation 2*b* in space group *Pbam* with point-group symmetry 2/*m* to a less constrained Wyckoff position 4*c* in space group *Pbnm* with point-group symmetry *m*. The indications for disorder vanished. The displacement can be used as the order parameter of the phase transition and it is accompanied by a strong kinking of the straight Ga2—O4—Ga2 angle (180° by symmetry in the low-pressure phase) between the $Ga2_2O_7$ tetrahedral dimers by ∼ 32° at 21.4 (5) GPa (Fig. 6). The DFT model clearly shows that in the athermal limit the displacement is a sudden change and that the phase transition is of first order (Fig. 6). However, Lopéz-de-la Torre *et al.* (2009) deduced that the phase transition is either tricritical or of first order from their earlier experimental findings. The ambiguity may be explained by either noting that the displacement of the O4 atom at finite temperatures may be relevant to the phase transition or that the resolution of the experimental data was insufficient. The kinking between the $Ga2_2O_7$ tetrahedral dimers results in the formation of two symmetrically independent GaO_4 tetrahedra (Fig. 7). Owing to the strong kinking the distance Ga2*B*—O2*A* is decreased, which is further enhanced on pressure increase. This tendency results in an increase of the coordination of one of the $Ga2O_4$ tetrahedra (Ga2*B*) to fivefold, forming a common edge with the $Ga1O_6$ octahedron. The kinking and increase of the Ga2*B* coordination are the response to the misfit of Ga^{3+} in tetrahedral coordination. By the increase of the Ga2*B* coordination the structural motif of groups of GaO_4 tetrahedra in the (001) plane changes towards zigzag chains of corner-connected $Ga2AO_4$ and $Ga2BO_5$ polyhedra running along the *b* direction (Fig. 7). The kinking of the $Ga2O_4$ tetrahedra is further expressed in strong changes of

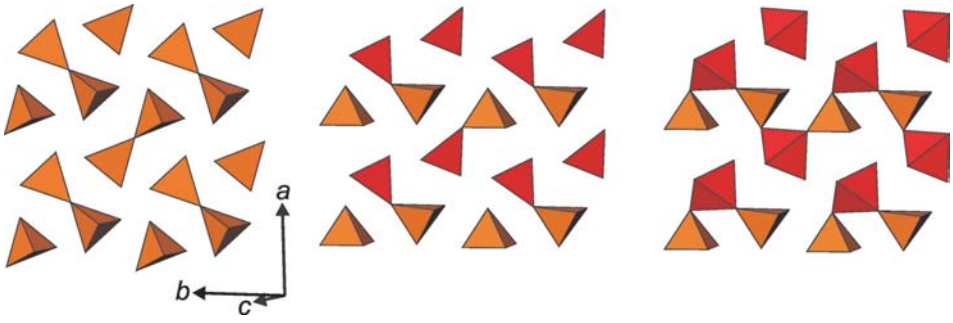

Figure 7
The $Ga2O_4$ tetrahedral layer in the crystal structure of the $Bi_2Ga_4O_9$ low-pressure phase at 14.9 (3) GPa (left) and of the high-pressure phase at 30.5 (5) GPa (center). In the high-pressure phase the Ga_2O_7 dimers are kinked, and two symmetry-non-equivalent polyhedra are distinguished. Right: Considering a fivefold coordination of the Ga2*B* atom, zigzag chains of Ga polyhedra are formed along the *b* axis. This figure is in colour in the electronic version of this paper.

the Bi—O3—Ga2 interpolyhedral angles, and especially in the increase of the Bi—O3*B*—Ga2*B* angle. A similar type of coordination change as that observed for Ga2*B* in $Bi_2Ga_4O_9$ was predicted for a phase transition of sillimanite to the high-pressure *meta*-sillimanite phase at 33.5–38 GPa by Oganov *et al.* (2001). At the transition pressure the Al—O and Si—O bonds of the AlO_4 and SiO_4 tetrahedra of sillimanite fall below a critical bonding distance such that the coordination is increased to fivefold for these Al and Si atoms. As no volume increase was allowed in these calculations, the transition was found to be isosymmetric, similar to the first calculations for $Bi_2Ga_4O_9$ in Lopéz-de-la Torre *et al.* (2009). The behaviour of the predicted lattice parameters also shows a similar tendency in sillimanite and $Bi_2Ga_4O_9$ with an anomalously large fall of the *a* parameter and an increase of the *c* parameter. Hence, the increase of the tetrahedral coordination by the formation of an additional bond at high pressure seems to be a general mechanism of the sillimanite-type structures.

The coordination of the Bi^{3+} cation increases at the phase transition from [4 + 2] to [6 + 1]. An additional bond is formed with the O4 atom, which is further shortened on increased pressure and is oriented parallel to the *c* axis. This is correlated with a displacement of the Bi position from a mirror plane, which is lost in the high-pressure phase, to a general position (Fig. 8). While in the ambient pressure phase the BiO_6 polyhedra are arranged in (001) planes alternating with planes of $Ga2_2O_7$ tetrahedra dimers connecting the $Ga1O_6$ octahedral chains, the BiO_7 polyhedra sheets are further connected along the *c* axis *via* the O4 atom in the high-pressure phase (Fig. 8). The increase of both the polyhedral Bi and Ga coordinations is accompanied by an increase of the polyhedral volumes, as it is expected (Fig. 4).

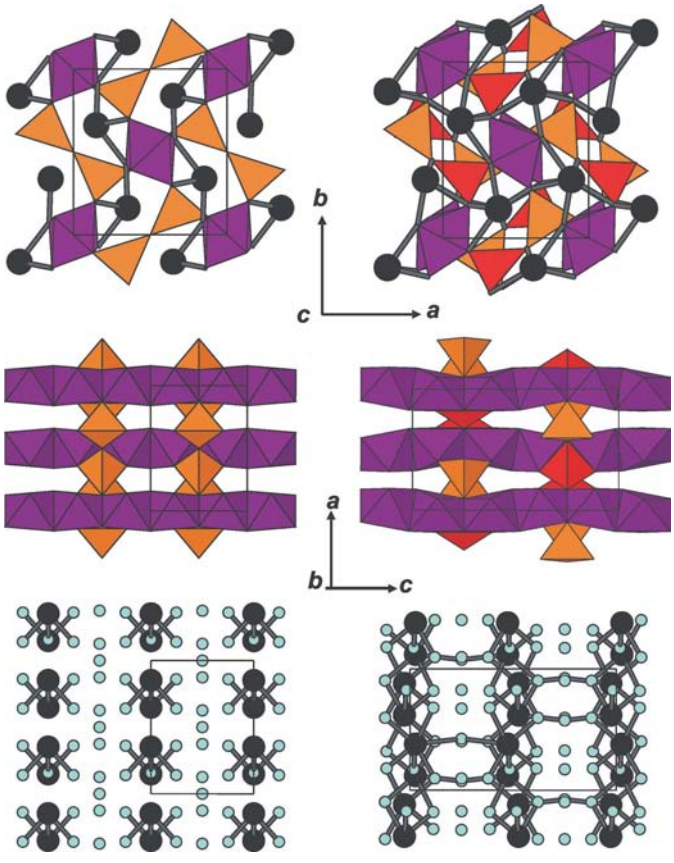

Figure 8
Crystal structures of the low-pressure phase of $Bi_2Ga_4O_9$ at 14.9 (3) GPa (left) and of the high-pressure phase at 30.5 (5) GPa (right). Only [4]- and [6]-fold coordinations of Ga are shown in the high-pressure structure for better comparison with the low-pressure structure. Different orientations show the connection of the GaO_6 octahedral chains *via* Ga_2O_7 groups (top) and the octahedral chains along the *c* axis with alternating sheets of Ga polyhedra (middle) and of Bi polyhedra (bottom) parallel to (001). This figure is in colour in the electronic version of this paper.

Owing to the symmetry reduction on the Ga1 special position (loss of the twofold rotation axis) the octahedral chains of GaO_6 octahedra along the *c* axis are kinked in the high-pressure phase, while they are straight in the low-pressure structure (Fig. 8). While the Ga1—O1—Ga1 angle across the common Ga octahedra edge O1—O1 hardly changes at the phase transition, the Ga1—O2—Ga1 angles across the common O2*A*—O2*B* edge change by an increase of the Ga1—O2*B*—Ga1 angle and a smaller decrease of the Ga1—O2*A*—Ga1 angle.

In general, all the Bi, Ga1, O1 and O4 atoms move from a special position in the low-pressure phase towards a general position, or a symmetry-reduced position for the O4 atom, in the high-pressure phase by the loss of part of the mirror planes perpendicular to the *c* axis, or loss of the twofold rotation axis parallel to the *c* axis for the O4 atom. With the elucidation of the mechanism of the phase transition we can confirm the assumption made by Lopéz-de-la Torre *et al.* (2009) that the unfavorable straight Ga2—O4—Ga2 angle of 180° cannot be maintained at high pressure. Hence, we expect that isotypic $Bi_2Fe_4O_9$ will show a similar phase transition at lower pressure than $Bi_2Ga_4O_9$, since Fe^{3+} has a slightly larger ionic radius (0.49 Å) than Ga^{3+} (0.47 Å, ionic radii for tetrahedral coordination of the cations; Shannon, 1976). High-pressure studies on $Bi_2Fe_4O_9$ are currently in progress. In contrast, isotypic $Bi_2Al_4O_9$ is stable up to at least 29 GPa (Lopéz-de-la Torre, 2009), which is consistent with the smaller ionic radius of Al^{3+} in tetrahedral coordination (0.39 Å; Shannon, 1976).

4.4. Compression of the high-pressure structure

Fitting a third-order Birch–Murnaghan equation-of-state to the pressure dependence of the unit-cell volume of the high-pressure phase in the pressure range from 16 to 50 GPa, as obtained from DFT data, results in V_0 = 803 (2) Å^3, B_0 = 75 (3) GPa and B' = 4.7 (1). As the magnitudes of the bulk modulus and its pressure derivative are correlated, the discussion will be limited to the results of fits with second-order Birch–Murnaghan equations-of-state, where B' = 4, for better comparison. The compressibility of the high-pressure phase [B_0 = 92.0 (7) GPa at B' = 4] is lower than that of the low-pressure phase [B_0 = 78.1 (9) GPa at B' = 4]. A comparison of the bulk moduli of the high-pressure phase obtained from DFT [B_0 = 92.0 (7) GPa at B' = 4] and from experiment

[B_0 = 89 (2) GPa at B' = 4; Lopéz-de-la Torre *et al.*, 2009] shows very good agreement.

The structural compression of the high-pressure phase shows a further decrease of the longest bonds in the Bi[6+1] and the Ga2*B*[4+1] coordinations, such that the bond lengths become more equal. This indicates that the increase of the coordination is not the driving force for the phase transition. As a result the eccentricity of the Bi^{3+} ion continues to decrease on pressure increase (Fig. 3) and the Bi atom continues to move in the same direction along the *a* axis on compression of the high-pressure phase, as in the low-pressure phase. Also, the corrugated chains ·—Bi—O—Bi—O—· running along the *b* axis behave in a similar way as in the low-pressure phase showing a further bending of the O1—Bi—O1′ angle and a straightening of the Bi—O1—Bi angle. This explains why the highest compressibility remains along the *a* axis in the high-pressure phase.

The overall polyhedral compression of the high-pressure phase obtained from theory agrees well with the experimental data, where only two pressure points are available at 21.4 (5) and 30.5 (5) GPa. Hence, the discussion is limited to the DFT data, where second-order Birch–Murnaghan equations-of-state have been fitted to the polyhedral volumes (Table 6). Again the BiO_7 polyhedron is the most compressible one with B_0 = 78 (4) GPa. The Ga2*A*O_4 tetrahedron is more compressible [$B_0 \simeq$ 157 (1) GPa] than the Ga2*B*O_5 polyhedron [$B_0 \simeq$ 241 (2) GPa] and the Ga1O_6 octahedron [$B_0 \simeq$ 248 (4) GPa], which show similar compressibility. While Ga2*B* and Ga1 polyhedra are more rigid in the high-pressure phase than in the low-pressure phase, the compressibility of the Ga2*A*O_4 tetrahedron is still similar to that of the GaO_4 tetrahedron in the low-pressure phase. As a larger compressibility of a polyhedron with a smaller coordination number is unusual, this leads to the assumption that another phase transition can be expected at higher pressure. This is also expected by analogy with the increase in all the SiO_4 and AlO_4 tetrahedra to fivefold coordination for the predicted metastable high-pressure phase of sillimanite when falling below a critical bonding distance (Oganov *et al.*, 2001).

4.5. The stereochemical activity of the lone electron pair

The lone electron pair is localized on one side of the Bi^{3+} ion pointing in the [110] direction towards the vacant position (Figs. 1 and 9). With increasing pressure the Bi^{3+} ion moves along the *a* axis and hence the lone electron pair moves towards the [010] direction. This movement is continued across the phase transition and in the high-pressure phase as the pressure increases (Fig. 9). Further, the spatial extension of the lone electron pair is strongly reduced up to 50 GPa and the shape is elongated in the direction away from Bi towards the [010] direction (Fig. 9). However, the DFT calculations clearly show that the lone electron pair is stable up to at least 50 GPa, in accordance with the crystal structure of the high-pressure phase. While the stereochemcial activity of Bi^{3+} is reduced at increasing pressure, a conversion of the lone electron pair into another electronic state, which would be accompanied by a symmetrization of the Bi coordination, was not observed in this pressure range. This shows an unexpected stability of the lone electron pair and of its stereochemical activity at high pressure in this compound. A similar stability was reported in PbO, where the lone electron pair of Pb^{2+} remained stable in the PbO high-pressure phases up to > 46 GPa (Häussermann *et al.*, 2001). In contrast, the lone electron pair of Pb^{2+} in Pb_3O_4 was assumed to adopt an almost pure *s*-type state in the high-pressure phase III at pressures above 6 GPa (Dinnebier *et al.*, 2003). A pressure-induced loss of stereochemical activity of

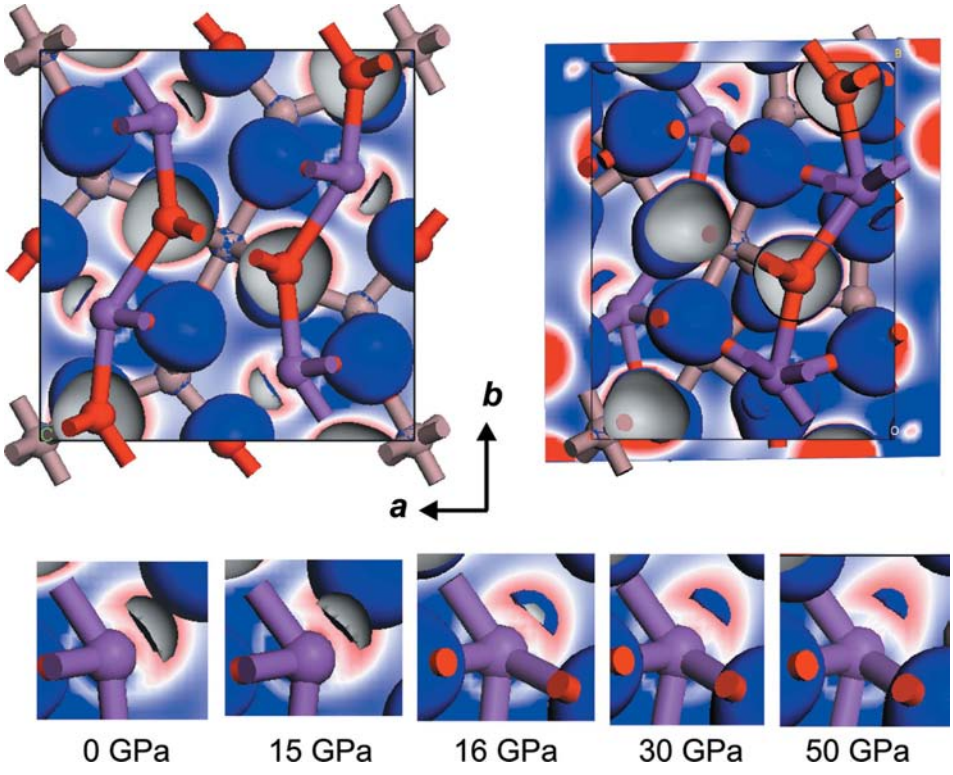

Figure 9
Calculated electron-density difference map and (001) slices at $z = 0$ for the low-pressure phase of $Bi_2Ga_4O_9$ and slices through the four Bi positions for the high-pressure phase, where they are slightly shifted away from $z = 0$, showing the position and size of the Bi^{3+} $6s^2$ lone electron pair at 0 GPa (top left) and at 50 GPa (top right). At the bottom the changes in the spatial extension, shape and position of the lone electron pair are shown for the low-pressure phase at 0 and 15 GPa (left), and for the high-pressure phase at 16, 30 and 50 GPa. The isosurface is based on an electron-density level of 0.038 e Å^{-3}. This figure is in colour in the electronic version of this paper.

the lone electron pair of Ge was also reported for $CsGeCl_3$ at ~ 5 GPa from DFT calculations (Winkler *et al.*, 1998). In SnO, a semiconductor-to-metal transition was observed at ~ 5 GPa and attributed to the closure of the indirect fundamental gap (Wang *et al.*, 2004).

4.6. Vibrational properties

The Raman spectra are plotted in Fig. 10. Relatively strong bands are observed at 201.5, 321.5, 357.5, 591.5 and 698.5 cm^{-1} at ambient conditions. Most of the Raman bands at wavenumbers $> 120\ cm^{-1}$, which were previously reported at ambient conditions (Beran *et al.*, 2008), were present in the Raman spectra of our single crystal loaded within the diamond–anvil cell. Hence, we refer to Beran *et al.* (2008) for the assignment of the Raman bands, except for a very weak, but distinct band, which we additionally observed at 208.5 cm^{-1}.

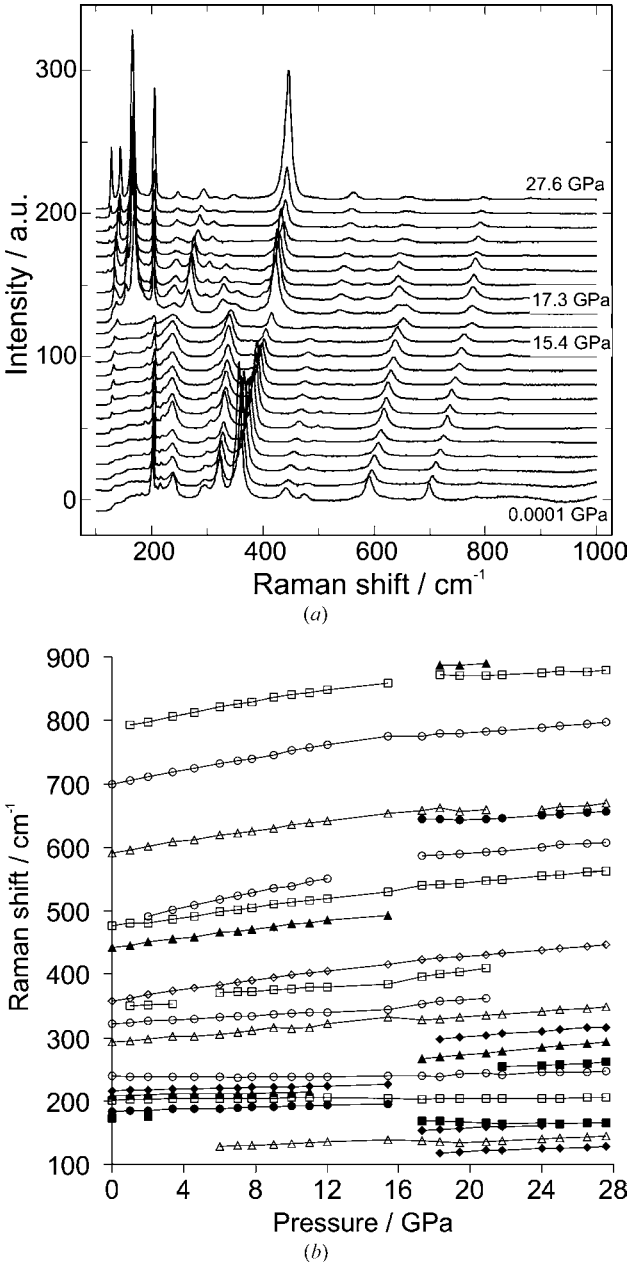

Figure 10
(*a*) Raman spectra of a $Bi_2Ga_4O_9$ single crystal at increasing pressure between 0.0001 and 27.6 (1) GPa. The phase transition occurs at about 16 GPa. (*b*) Pressure dependencies of the Raman bands.

The mode-Grüneisen parameter γ was calculated for each vibrational mode i of the low-pressure phase in the pressure range up to the phase transition according to: $\gamma_i = B_0(d\nu_i/dp)/\nu_{i0}$, where B_0 is the isothermal bulk modulus, ν is the frequency and p is the pressure. For the bulk modulus we used the experimental value of 102 GPa (Lopéz-de-la Torre *et al.*, 2009). The values for ν_{i0} were obtained from our Raman spectrum at ambient pressure or from Beran *et al.* (2008). With increasing pressure all Raman bands shift towards higher frequencies, *i.e.* show positive mode-Grüneisen parameters. Only the Bi—O stretching mode at 239 cm^{-1} does not show a distinct pressure shift up to the phase transition at 16 GPa ($\gamma = 0.01$). The blue shift with increasing pressure is less pronounced in the Bi—O vibrations ($0.01 < \gamma < 0.94$) compared with the Ga—O modes ($0.45 < \gamma < 1.25$). Starting at a pressure above 1 GPa, the Raman band at 481.2 cm^{-1} [at 2.0 (1) GPa] forms a shoulder. This results in a pressure-induced splitting of the ν_3 Ga—O stretching mode, which is associated with the GaO_6 octahedron. The largest γ are observed for one of the ν_3 Ga—O stretching modes ($\gamma = 1.25$), the ν_2 Ga—O stretching mode at 357.5 cm^{-1} ($\gamma = 1.09$), and the Bi—O—Bi bending mode at 122 cm^{-1} ($\gamma = 0.94$; Fig. 10). The γ values are comparable to the typical γ values of silicates. For example, structurally related sillimanite shows γ values between 0.29 and 1.93 with typical values from 0.7 to 1.0, besides some negative mode-Grüneisen parameters (Menargh & Liu, 1991). For the Al_2SiO_5 polymorph andalusite γ ranges between 0.72 and 1.13 (Menargh & Liu, 1991).

While the low-pressure phase of $Bi_2Ga_4O_9$ has 87 optical modes (Beran *et al.*, 2008), the doubling of the unit cell in the high-pressure phase (60 atoms in the primitive cell) results in a total number of 180 vibrational modes. According to group theory, 90 modes are Raman-active: $\Gamma_{Ra} = 25\ A_g + 20\ B_{1g} + 25\ B_{2g} + 20\ B_{3g}$, 70 modes are IR-active: $\Gamma_{IR} = 25\ B_{1u} + 20\ B_{2u} + 25\ B_{3u}$, of which three modes are acoustic ($1B_{1u} + 1\ B_{2u} + 1\ B_{3u}$), and 20 A_u modes are both Raman- and IR-inactive. At the phase transition small changes are observed in the Raman spectra. This is consistent with the small structural displacements occurring at the phase transition. Two new Raman bands are observed in the region of the Bi—O stretching and bending modes, a weak one at 154 cm^{-1} and a very strong band at 169 cm^{-1} [both at 17.3 (1) GPa]. As the pressure increases the Bi—O stretching mode at 245 cm^{-1} [at 21.8 (1) GPa] forms a shoulder (at 255 cm^{-1}). At the phase transition a strong Raman band appears at 266 cm^{-1} [at 17.3 (1) GPa], and a very weak one can be distinguished at 298 cm^{-1} [at 18.4 (2) GPa]. The Ga2—O4—Ga2 bending mode of the GaO_4 tetrahedra shows a splitting into a doublet at 17.3 (1) GPa (644 and 657 cm^{-1}), which might be due to the strong kinking of this inter-tetrahedra angle at the phase transition. Another splitting is observed for the Ga—O

stretching mode of the GaO_4 tetrahedra parallel to [001] [871.5 and 886.4 cm^{-1} at 18.4 (2) GPa], which again might be due to two distinct $Ga2O_4$ tetrahedra in the high-pressure structure. Raman bands, which can only be observed at pressures below the phase transition, but not in the high-pressure phase, are the weak bands at 183, 208.3 and 215.6 cm^{-1}, and the stronger one at 442 cm^{-1} (values given at 0.0001 GPa). A more detailed assignment of the changes of the lattice dynamics at the phase transition would require time-intensive computations, which were outside of the scope of the present study.

5. Conclusions

From experiments and DFT model calculations we have determined the compression mechanisms of the lone electron pair compound $Bi_2Ga_4O_9$ across the pressure-induced structural phase transition at 16 GPa. It was found that the stereochemical activity of the Bi^{3+} $6s^2$ lone electron pair persists up to the maximum pressure of 50 GPa. This is confirmed by the remaining eccentricity of the Bi^{3+} ion, as observed experimentally in the high-pressure phase, and by the DFT model, where the lone electron pair remains localized. The compression of both the low- and the high-pressure structures of $Bi_2Ga_4O_9$ are dominated by the compression of the Bi environment, which is reflected in the strong decrease of the BiO_6 polyhedral volume, the decreasing eccentricity of the Bi^{3+} ion, and its shift along the *a* axis. The position of the localized lone electron pair changes on increasing pressure, its spatial extension is reduced and its shape is elongated. The high-pressure phase transition at 16 GPa is due to a symmetry-breaking displacement of the O4 atom accompanied by a kinking of the straight Ga2—O4—Ga2 angle between the Ga_2O_7 tetrahedral dimers, which is a response to the misfit of Ga^{3+} in tetrahedral coordination. At least in the athermal limit the phase transition is of first order. The crystal structure of the high-pressure phase shows an increase of the coordination of one GaO_4 tetrahedron to $Ga^{[4+1]}O_5$ and of the $Bi^{[4+2]}O_6$ polyhedron to $Bi^{[6+1]}O_7$. Raman spectroscopy shows small changes in the lattice dynamics ($\gamma < 1.25$ in the low-pressure phase), consistent with findings from diffraction. However, as a few notable changes are present, like the appearance of a very strong Raman band at 169 cm^{-1} in the high-pressure phase, lattice dynamics can be used to further understand the structural phase transition. As a tetrahedral coordination is even more unfavorable for Fe^{3+}, we predict a high-pressure phase transition to occur in the isotypic $Bi_2Fe_4O_9$ at lower pressure. High-pressure studies on $Bi_2Fe_4O_9$ are currently in progress.

This research was supported by Deutsche Forschungsgemeinschaft, Germany, within the projects SPP1136 (WI1232/17-2), SPP1236 (WI1232/25-1 and FR2491/2-1), and PAK279 (MU1006/8-1). Thanks are due to HASYLAB for synchrotron beamtime and financial support. A. Friedrich thanks the Christiane-Nüsslein-Volhard-Stiftung and the Goethe University Frankfurt (program 'junior research scientists in focus') for support.

References

Abrahams, I., Bush, A. J., Hawkes, G. E. & Nunes, T. (1999). *J. Solid State Chem.* **147**, 631–636.
Angel, R. J. (2003). *J. Appl. Cryst.* **36**, 295–300.
Angel, R. J. (2004). *J. Appl. Cryst.* **37**, 486–492.
Balić Žunić, T. & Makovicky, E. (1996). *Acta Cryst.* B**52**, 78–81.
Balić Žunić, T. & Vicković, I. (1996). *J. Appl. Cryst.* **29**, 305–306.
Beran, A., Libowitzky, E., Burianek, M., Mühlberg, M., Pecharróman, C. & Schneider, H. (2008). *Cryst. Res. Technol.* **43**, 1230–1239.
Blasse, G. & Ho, O. B. (1980). *J. Lumin.* **21**, 165–168.
Bloom, I., Hash, M. C., Zebrowski, J. P., Myles, K. M. & Krumpelt, M. (1992). *Solid State Ion.* **53–56**, 739–747.
Boehler, R. (2006). *Rev. Sci. Instrum.* **77**, 115103.
Boehler, R. & de Hantsetter, K. (2004). *High Pressure Res.* **24**, 391–396.
Burianek, M., Mühlberg, M., Woll, M., Schmücker, M., Gesing, T. M. & Schneider, H. (2009). *Cryst. Res. Technol.* **44**, 1156–1162.
Burla, M. C., Caliandro, R., Camalli, M., Carrozzini, B., Cascarano, G. L., De Caro, L., Giacovazzo, C., Polidori, G. & Spagna, R. (2005). *J. Appl. Cryst.* **38**, 381–388.
Burt, J. B., Ross, N. L., Angel, R. J. & Koch, M. (2006). *Am. Mineral.* **91**, 319–326.
Clark, S. J., Segall, M. D., Pickard, C. J., Hasnip, P. J., Probert, M. J., Refson, K. & Payne, M. C. (2005). *Z. Kristallogr.* **220**, 567–570.
Dinnebier, R. E., Carlson, S., Hanfland, M. & Jansen, M. (2003). *Am. Mineral.* **88**, 996–1002.
Dowty, E. (2000). *ATOMS for Windows*, Version 5.1. Shape Software, Kingsport, USA.
Eichhorn, K. (1978). *AVSORT*. HASYLAB/DESY, Hamburg, Germany.
Eichhorn, K. (1987). *REDUCE*. HASYLAB/DESY, Hamburg, Germany.
Farrugia, L. J. (1999). *J. Appl. Cryst.* **32**, 837–838.
Filatov, S. K., Krivovichev, S. V., Aleksandrova, Y. V., Bubnova, R. S., Egorysheva, A. V., Burns, P., Kargin, Y. F. & Volkov, V. V. (2006). *Russ. J. Inorg. Chem.* **51**, 878–883.
Finger, L. W. & King, H. E. (1978). *Am. Mineral.* **63**, 337–342.
Fischer, R. X. & Schneider, H. (2005). *Mullite*, edited by H. Schneider & S. Komarneni, pp. 1–140. Weinheim: Wiley-VCH.
Halasyamani, P. S. & Poeppelmeier, K. R. (1998). *Chem. Mater.* **10**, 2753–2769.
Häussermann, U., Berastegui, P., Carlson, S., Haines, J. & Léger, J.-M. (2001). *Angew. Chem. Int. Ed.* **40**, 4624–4629.
Hazen, R. M., Downs, R. T. & Prewitt, C. T. (2000). *High-Temperature and High-Pressure Crystal Chemistry*, edited by R. M. Hazen & R. T. Downs, Vol. 41, pp. 1–33. Washington DC: Mineralogical Society of America.
Kerrick, D. M. (1990). *Reviews in Mineralogy*, edited by P. H. Ribbe, Vol. 22, pp. 1–406. Washington DC: Mineralogical Society of America.
Lopéz-de-la Torre, L., Friedrich, A., Juarez-Arellano, E. A., Winkler, B., Wilson, D. J., Bayarjargal, L., Hanfland, M., Burianek, A., Mühlberg, M. & Schneider, H. (2009). *J. Solid State Chem.* **182**, 767–777.
Lundegaard, L. F., Makovicky, E., Boffa-Ballaran, T. & Balic Zunic, T. (2005). *Phys. Chem. Miner.* **32**, 578–584.
Lundegaard, L. F., Miletich, R., Balic Zunic, T. & Makovicky, E. (2003). *Phys. Chem. Miner.* **30**, 463–468.
Mao, H. K., Xu, J. & Bell, P. M. (1986). *J. Geophys. Res.* **91**, 4673–4676.
Menargh, T. P. & Liu, L.-G. (1991). *Phys. Chem. Miner.* **18**, 126–130.
Miletich, R., Allan, D. R. & Kuhs, W. F. (2000). *High-Temperature and High-Pressure Crystal Chemistry*, edited by R. M. Hazen & R.

T. Downs, Vol. 41, pp. 445–520. Washington DC: Mineralogical Society of America.
Milman, V., Akhmatskaya, E. V., Nobes, R. H., Winkler, B., Pickard, C. J. & White, J. A. (2001). *Acta Cryst.* B**57**, 163–177.
Mueller-Buschbaum, H. & de Beaulieu, D. C. (1978). *Z. Naturforsch. B*, **33**, 669–670.
Oganov, A. R., Price, G. D. & Brodholt, J. P. (2001). *Acta Cryst.* A**57**, 548–557.
Olsen, L. A., Balić-Zunić, T. & Makovicky, E. (2008). *Inorg. Chem.* **47**, 6756–6762.
Olsen, L. A., Balic Zunic, T., Makovicky, E., Ullrich, A. & Miletich, R. (2007). *Phys. Chem. Miner.* **34**, 467–475.
Oxford Diffraction (2007). *CrysAlis*. Oxford Diffraction Ltd, Abingdon, England.
Perdew, J. P., Burke, K. & Ernzerhof, M. (1996). *Phys. Rev. Lett.* **77**, 3865–3868.
Ralph, R. L., Finger, L. W., Hazen, R. M. & Ghose, S. (1984). *Am. Mineral.* **69**, 513–519.
Safronov, G. M., Speranskaya, E. I., Batog, V. N. & Mitkina, G. D. (1971). *Zh. Neorg. Khim. Russ.* **16**, 526.
Schreuer, J., Burianek, M., Mühlberg, M., Winkler, B., Wilson, D. J. & Schneider, H. (2006). *J. Phys. Condens. Matter*, **18**, 10977–10988.
Shannon, R. D. (1976). *Acta Cryst.* A**32**, 751–767.
Sheldrick, G. M. (2008). *Acta Cryst.* A**64**, 112–122.
Syassen, K. (2005). *DATLAB*, Version 1.37d. MPI/FKF Stuttgart, Germany.
Temple, P. A. & Hathaway, C. E. (1973). *Phys. Rev. B*, **7**, 3685–3697.
Tutov, A. G. & Markin, V. N. (1970). *Izv. Akad. Nauk SSSR Neorg. Mater.* **6**, 2014–2017.
Volkov, V. V. & Egorysheva, A. V. (1996). *Opt. Mater.* **5**, 273–277.
Volkov, V. V., Egorysheva, A. V., Kargin, Y. F., Solomonov, V. I., Mikhailov, S. G., Buzmakova, S. I., Shul'gin, B. V. & Skorikov, V. M. (1996). *Inorg. Mater.* **32**, 455–458.
Wang, X., Zhang, F., Loa, I., Syassen, K., Hanfland, M. & Mathis, Y.-L. (2004). *Phys. Status Solidi. (B)*, **241**, 3168–3178.
Winkler, B., Milman, V. & Lee, M.-H. (1998). *J. Chem. Phys.* **108**, 5506–5509.
Yang, H., Downs, R. T., Finger, L. W., Hazen, R. M. & Prewitt, C. T. (1997*a*). *Am. Mineral.* **82**, 467–474.
Yang, H., Hazen, R. M., Finger, L. W., Prewitt, C. T. & Downs, R. T. (1997*b*). *Phys. Chem. Miner.* **25**, 39–47.
Zha, S., Cheng, J., Liu, Y., Liu, X. & Meng, G. (2003). *Solid State Ion.* **156**, 197–200.
Zhang, L., Ahsbahs, H. & Kutoglu, A. (1998). *Phys. Chem. Miner.* **25**, 301–307.